Solar Flare Spectroscopic Diagnostics for Wavelengths Less Than 2000 Angstroms

G. A. DOSCHEK AND U. FELDMAN

Space Science Division

NAVAL RESEARCH LABORATORY
Washington, D.C.

REPORT DOCUMENTATION PAGE		READ INSTRUCTIONS BEFORE COMPLETING FORM
1. REPORT NUMBER NRL Report 8307	2. GOVT ACCESSION NO.	3. RECIPIENT'S CATALOG NUMBER
4. TITLE (and Subtitle) SOLAR FLARE SPECTROSCOPIC DIAGNOSTICS FOR WAVELENGTHS LESS THAN 2000 ANGSTROMS		5. TYPE OF REPORT & PERIOD COVERED Interim report on a continuing NRL Problem
		6. PERFORMING ORG. REPORT NUMBER
7. AUTHOR(s) G.A. Doschek and U. Feldman		8. CONTRACT OR GRANT NUMBER(s)
9. PERFORMING ORGANIZATION NAME AND ADDRESS Naval Research Laboratory Washington, DC 20375		10. PROGRAM ELEMENT, PROJECT, TASK AREA & WORK UNIT NUMBERS NRL Problem A01-24A Project NASA DPRS-60404-6
11. CONTROLLING OFFICE NAME AND ADDRESS National Aeronautical and Space Administration Washington, DC 20546		12. REPORT DATE June 27, 1979
		13. NUMBER OF PAGES 32
14. MONITORING AGENCY NAME & ADDRESS(if different from Controlling Office)		15. SECURITY CLASS. (of this report) UNCLASSIFIED
		15a. DECLASSIFICATION/DOWNGRADING SCHEDULE

16. DISTRIBUTION STATEMENT (of this Report)

Approved for public release; distribution unlimited

17. DISTRIBUTION STATEMENT (of the abstract entered in Block 20, if different from Report)

18. SUPPLEMENTARY NOTES

Given as an invited review paper at the Workshop on Solar Flare Research and the Solar Maximum Mission, Ann Arbor, Michigan, 14-16 November 1978.

19. KEY WORDS (Continue on reverse side if necessary and identify by block number)

Solar flares
EUV spectrum analysis
Electron density and temperature

20. ABSTRACT (Continue on reverse side if necessary and identify by block number)

We discuss the use of intensity ratios of emission lines for determining the electron density and temperature in flare plasmas. The availability diagnostics cover the temperature range from about 4×10^4 K to about 10^7 K. We summarize the current work on flare density diagnostics and review the applications of this theory to available flare spectra. We discuss the importance of line profiles for determining nonthermal mass motions in the plasma and for estimating path lengths along the line of sight. We review the current information on line profiles in flare spectra. We comment on determining departures from ionization equilibrium using line ratios in the x-ray and EUV regions.

DD $_{1\ JAN\ 73}^{FORM}$ 1473 EDITION OF 1 NOV 65 IS OBSOLETE
S/N 0102-014-6601

CONTENTS

SOLAR FLARE SPECTROSCOPIC DIAGNOSTICS FOR
WAVELENGTHS LESS THAN 2000 ANGSTROMS

INTRODUCTION

In this review we discuss spectroscopic diagnostics for solar flares for wavelengths less than 2000 Å. We review the application of these diagnostics to the available data and summarize the results. We confine our attention to the emission line spectrum and summarize what can be learned about the physical conditions in flare plasmas from line intensities and profiles.

The discussion of the flare spectrum can be conveniently subdivided according to the wavelength ranges accessible to different types of instrumentation. These ranges are determined by various instrumental parameters such as the type of diffracting element, the angles of incidence, or the coatings on optical surfaces.

The region from ≈1150 to ≈2000 Å is covered by normal-incidence spectrographs. The lower wavelength cutoff is due to the MgF_2 coating used on optical surfaces. A fairly large data base for flares exists for this spectral region. These data were obtained from the NRL slit spectrograph flown on Skylab [1]. The spectral resolution of that instrument was 0.06 Å, which is more than adequate for obtaining profiles in this wavelength region for all lines formed above ≈2×10^4 K. The spatial resolution was 2 seconds by 60 seconds at sun center, and spectra were recorded on Kodak 104 and 101 film.

The spectrum down to ≈170 Å can also be observed using normal-incidence spectrographs. The lower wavelength cutoff is determined by the decreasing reflectivity of short-wavelength radiation at normal incidence. The region from ≈170 to ≈600 Å was covered by the NRL slitless spectrograph on Skylab [2]. The spatial resolution was about 3 seconds near 300 Å. Spectral resolution is difficult to specify for this instrument, because images of the plasma, rather than spectral lines, were recorded. However, for small flares the spectral resolution was sufficiently good that blending of images is usually not a problem. A number of flare spectra were obtained, as reported by Widing and Dere [3] and by others. In addition to the NRL instrument, the Harvard College Observatory (HCO) spectroheliometer on Skylab covered the wavelength region from 280 to 1350 Å, with a spectral resolution of 1.6 Å [4]. Several flare spectra were obtained. Because of the low spectral resolution, most of the lines are blended, and the spectroscopic diagnostics we discuss in this paper cannot be applied to the HCO data.

The spectral regions below 170 Å must be studied using grazing incidence or Bragg crystal instruments. The region from ≈9 to ≈170 Å can be studied using grazing-incidence spectrographs. Actually one can observe the entire wavelength region from 9 to 800 Å using grazing-incidence instrumentation. Excluding the x-ray region below 40 Å, the solar spectrum

below 170 Å has not been adequately explored. The only data with sufficient spectral resolution for measurements of line profiles have been quiet-sun spectra obtained by rocket spectrographs, as obtained by Behring, Cohen, and Feldman [5] and by others. The only available flare spectra were recorded by the Goddard Space Flight Center (GSFC) spectrometer flown on OSO-5 [6]. This instrument covered the wavelength region from 25 to 400 Å with a spectral resolution of ≈ 0.7 Å. The instrument was a scanning spectrometer; that is, the grating rotated, and different wavelengths were recorded at different times. Neither the time resolution nor spectral resolution is adequate for application of most of the worthwhile spectral diagnostics, and there was no spatial resolution. This neglected spectral region should be observed by a high-resolution instrument flown on the shuttle. However, although the GSFC instrument was a first-generation spectrometer, the information on flare spectra obtained from the data has been invaluable for designing a more sophisticated instrument and has been the basis of several of the diagnostic possibilities we will discuss.

Below ≈ 40 Å (the x-ray region) the available flare spectra have been recorded by Bragg crystal spectrometers. Such instruments were flown by GSFC on OSO-3 [7] and OSO-5 [8] and by NRL on OSO-4 and OSO-6 [9]. The spectral resolution of all these instruments was inadequate to exploit the spectroscopic techniques that were subsequently developed by analyzing and identifying the lines in the spectra. More recently spectrometers with higher time resolution were flown by Columbia University on OSO-8 [10]. Again, the spectral resolution is inadequate, although the time resolution is not bad for the thermal x-ray flare emission (≈ 10 s). None of these Bragg crystal spectrometers have any spatial resolution. The only flare spectra with adequate spectral resolution were obtained by Mandelstam and his colleagues at the Lebedev Physical Institute in Moscow [11]. These data have stimulated considerable theoretical activity in the interpretation of satellite lines of hydrogenlike and heliumlike ions that will be invaluable for interpreting the x-ray spectra from the Solar Maximum Mission.

We summarize these comments by concluding that although numerous flare spectra have been recorded below 2000 Å, most of the spectra, particularly at the shorter wavelengths, do not have the spectral, spatial, or temporal resolution necessary to fully realize the diagnostic potential of the emission line spectrum.

SPECTROSCOPIC DIAGNOSTICS FOR FLARES

The thermal flare plasma is known to consist of regions of different temperatures. During a flare, enhancements of EUV and x-ray emission come from the flaring chromosphere, transition zone, and corona. We confine our attention here to the portion of the atmosphere between about 2×10^4 K (the upper chromosphere or the lower transition zone) and about 30×10^6 K (approximately the highest temperature that has been deduced for the thermal coronal plasma). The distribution of ionization states formed within this temperature range in flare plasmas is determined primarily by the balance between ionization by electron collisions and radiative and dielectronic recombination. As a general rule, resonance lines formed at lower temperatures fall toward longer wavelengths. Thus at first sight it would appear that the highest-temperature regions of flare plasmas are best observed in the x-ray region. Although this is true for the very highest temperature regions, that is, the regions that produce Fe XXV, Fe XXVI, and Ca XX lines in the x-ray region, temperature regions in excess of 20×10^6 K can be observed at longer wavelengths, even longer than

1000 Å. Figure 1 shows an energy-level diagram for a typical ion, Fe XXII. In the x-ray region, innershell emission between the $n = 1$ and $n = 2$ principal quantum levels ($\Delta n = 1$) occurs near 1.9 Å. Also in the x-ray region, lines due to $2s^2 2p - 2s^2 3\ell$ transitions (also $\Delta n = 1$) are formed near 11.6 Å. However, the $\Delta n = 0$ transitions of the type $2s^2 2p - 2s2p^2$ fall near 110 Å, and the forbidden line $2s^2 2p\ ^2P_{1/2} - 2s^2 2p\ ^2P_{3/2}$ falls at 845 Å. A similar situation holds for most of the iron ions from Fe XVIII through Fe XXIV. The innershell lines are grouped together between ≈ 1.86 and 1.9 Å, other $\Delta n = 1$ transitions occur between ≈ 7 and ≈ 15 Å, and most of the $\Delta n = 0$ transitions occur between ≈ 90 and ≈ 300 Å. Most of the strong $\Delta n = 0$ lines of Fe XVIII through Fe XXIII fall shortward of 160 Å. However, the Fe XXIV lines fall at 192 and 255 Å, and some transitions of Fe XIX through Fe XXIII also fall longward of 170 Å. Forbidden lines arising from transitions within a term in the ground configuration fall longward of 800 Å, and transitions between different terms in the ground configuration fall shortward of 800 Å. Thus, many of the $\Delta n = 0$ lines can be observed with either grazing-incidence or normal-incidence instruments. A complete list of all the known iron lines due to $\Delta n = 0$ transitions is given in Table 1. Because of blending of the $\Delta n = 1$ transitions in the x-ray region, it is not presently possible to present a similar list of these lines.
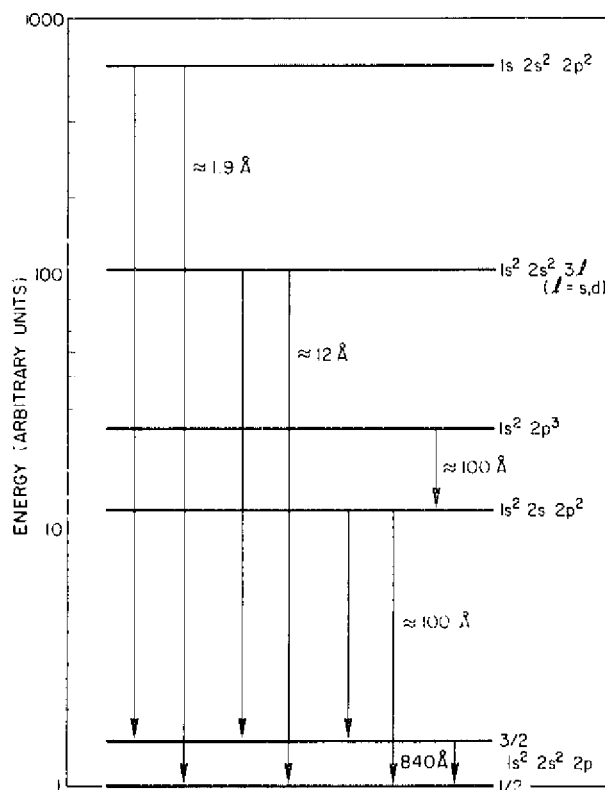

Fig. 1 — Approximate energy-level diagram for Fe XXII showing where the main groupings of iron lines appear in the x-ray and EUV spectrum

Table 1 — Iron Lines of Fe XVII Through Fe XXIV.
Wavelength values in parentheses are predicted values.

Transition			λ (Å)	Ref.
Fe XVIII				
$2s^2 2p^5\ ^2P_{3/2}$	— $2s2p^6$	$^2S_{1/2}$	93.93	12
$^2P_{1/2}$	—	$^2S_{1/2}$	103.95	12
$2s^2 2p^5\ ^2P_{3/2}$	— $2s^2 2p^5$	$^2P_{1/2}$	974.8	13
Fe XIX				
$2s^2 2p^4\ ^3P_2$	— $2s2p^5$	$^1P_1$	78.88	14
$^3P_2$	—	$^1P_1$	83.85	14
$^3P_0$	—	$^1P_1$	84.87	14
$^1D_2$	—	$^1P_1$	91.02	15
$^3P_2$	—	$^3P_1$	101.56	15
$^1S_0$	—	$^1P_1$	106.12	15
$^3P_1$	—	$^3P_0$	106.33	15
$^3P_2$	—	$^3P_2$	108.37	15
$^3P_0$	—	$^3P_1$	109.97	15
$^3P_1$	—	$^3P_1$	111.70	15
$^3P_1$	—	$^3P_2$	120.00	15
$2s2p^5\ ^1P_1$	— $2p^6$	$^1S_0$	115.42	16
$2s^2 2p^4\ ^3P_1$	— $2s^2 2p^4$	$^1S_0$	424.26	17
$^3P_2$	—	$^1D_2$	592.16	18
$^3P_2$	—	$^3P_1$	1118.1	13
$^3P_2$	—	$^3P_0$	(1328.1)	15
$^3P_0$	—	$^3P_1$	(7084)	15
Fe XX				
$2s^2 2p^3\ ^2D_{3/2}$	— $2s2p^4$	$^2P_{1/2}$	83.24	19
$^2D_{3/2}$	—	$^2P_{3/2}$	90.60	19
$^2P_{1/2}$	—	$^2P_{1/2}$	(92.63)	20
$^2D_{5/2}$	—	$^2P_{3/2}$	93.78	16,19
$^2D_{3/2}$	—	$^2S_{1/2}$	94.65	21
$^2P_{3/2}$	—	$^2P_{1/2}$	98.37	19
$^2P_{1/2}$	—	$^2P_{3/2}$	101.83	19
$^2P_{1/2}$	—	$^2S_{1/2}$	106.97	21
$^2P_{3/2}$	—	$^2P_{3/2}$	108.81	19
$^2D_{3/2}$	—	$^2D_{3/2}$	110.64	16,19
$^2D_{5/2}$	—	$^2D_{5/2}$	113.36	16,19
$^2P_{3/2}$	—	$^2S_{1/2}$	(114.67)	19
$^2D_{5/2}$	—	$^2D_{3/2}$	115.39	20
$^4S_{3/2}$	—	$^4P_{1/2}$	118.66	19
$^4S_{3/2}$	—	$^4P_{3/2}$	121.83	16,19
$^2P_{1/2}$	—	$^2D_{3/2}$	(127.85)	19
$^4S_{3/2}$	—	$^4P_{3/2}$	132.85	16,19
$^2P_{3/2}$	—	$^2D_{5/2}$	136.06	20

Table continues.

4

Table 1 (Continued) -- Iron Lines of Fe XVII Through Fe XXIV.
Wavelength values in parentheses are predicted values.

Transition	$\lambda(\text{Å})$	Ref.
Fe XX (Continued)		
$2s2p^4\ ^2D_{3/2} - 2p^5\ ^2P_{1/2}$	98.09	22
$^2D_{3/2} - {}^2P_{3/2}$	109.68	22
$^2D_{3/2} - {}^2P_{3/2}$	111.60	22
$^2D_{5/2} - {}^2P_{3/2}$	122.00	20
$^2P_{3/2} - {}^2P_{1/2}$	131.76	20
$^2S_{1/2} - {}^2P_{3/2}$	138.49	20
$^2P_{1/2} - {}^2P_{1/2}$	140.42	20
$2s^2 2p^3\ ^4S_{3/2} - 2s^2 2p^3\ ^2P_{3/2}$	326.76	17
$^4S_{3/2} - {}^2P_{1/2}$	411.61	17
$^2D_{3/2} - {}^2P_{3/2}$	541.35	17
$^4S_{3/2} - {}^2D_{5/2}$	(629.9)	17
$^4S_{3/2} - {}^2D_{3/2}$	(824.1)	17
$^2D_{5/2} - {}^2D_{3/2}$	2665.1	23
Fe XXI		
$2s^2 2p^2\ ^3P_0 - 2s2p^3\ ^3S_1$	91.28	21
$^3P_1 - {}^3S_1$	97.87	21
$^1D_2 - {}^1P_1$	98.37*	21
$^3P_2 - {}^3S_1$	102.21	21
$^3P_0 - {}^3P_1$	108.45	20
$^1S_0 - {}^1P_1$	112.47	20
$^1D_2 - {}^1D_2$	113.31	21
$^3P_1 - {}^3P_2$	115.16	20
$^3P_1 - {}^3P_1$	117.89	20
$^3P_1 - {}^3P_0$	118.70	20
$^3P_2 - {}^3P_2$	121.16	21
$^3P_2 - {}^3P_1$	(124.25)	20
$^3P_0 - {}^3D_1$	128.73	20
$^3P_1 - {}^3D_2$	142.14	20
$^3P_2 - {}^3D_3$	145.66	20
$^3P_2 - {}^3D_2$	151.51	20
$^3P_1 - {}^5S_2$	242.07	24
$^3P_2 - {}^5S_2$	270.52*	24
$2s2p^3\ ^1P_1 - 2p^4\ ^1S_0$	125.30	20
$^1D_2 - {}^1D_2$	144.82	20
$2s^2 2p^2\ ^3P_1 - 2s^2 2p^2\ ^1S_0$	330.23	17
$^3P_1 - {}^1D_2$	567.76	17
$^3P_2 - {}^1D_2$	(753.5)	17
$^3P_0 - {}^3P_1$	1354.1	13
$^3P_1 - {}^3P_2$	(2304)	13

* Blend

Table continues.

Table 1 (Concluded) — Iron Lines of Fe XVII Through Fe XXIV.
Wavelength values in parentheses are predicted values.

Transition	$\lambda(\text{Å})$	Ref.
Fe XXII		
$2s^2 2p$ $^2P_{1/2}$ — $2s2p^2$ $^2P_{3/2}$	100.77	25,26
$^2P_{1/2}$ — $^2P_{1/2}$	102.23	20
$^2P_{3/2}$ — $^2P_{3/2}$	114.39	25,26
$^2P_{3/2}$ — $^2P_{1/2}$	116.29	20
$^2P_{1/2}$ — $^2S_{1/2}$	117.17	20
$^2P_{1/2}$ — $^2D_{3/2}$	135.78	20
$^2P_{3/2}$ — $^2S_{1/2}$	(136.01)	20
$^2P_{3/2}$ — $^2D_{5/2}$	155.87	20
$^2P_{3/2}$ — $^2D_{3/2}$	(161.75)	20
$^2P_{1/2}$ — $^4P_{3/2}$	217.30	27
$^2P_{1/2}$ — $^4P_{3/2}$	247.19	27
$^2P_{1/2}$ — $^4P_{1/2}$	253.17	27
$^2P_{3/2}$ — $^4P_{5/2}$	292.46	27
$^2P_{3/2}$ — $^4P_{3/2}$	349.3*	27
$2s2p^2$ $^4P_{3/2}$ — $2p^3$ $^4S_{3/2}$	117.52	20
$^4P_{1/2}$ — $^4S_{3/2}$	125.71	20
$^4P_{3/2}$ — $^4S_{3/2}$	134.65	20
$^2S_{5/2}$ — $^2P_{3/2}$	139.82	20
$^2S_{1/2}$ — $^2P_{1/2}$	144.82	20
$^2D_{3/2}$ — $^2D_{5/2}$	149.90	20
$^2D_{5/2}$ — $^2D_{5/2}$	156.84	20
$^2D_{5/2}$ — $^2D_{3/2}$	157.36	20
$2s^2 2p$ $^2P_{1/2}$ — $2s^2 2p$ $^2P_{3/2}$	845.1	28
Fe XXIII		
$2s^2$ $^1S_0$ — $2s2p$ $^1P_1$	132.83	6
$^1S_0$ — $^3P_1$	263.76	29
Fe XXIV		
$2s$ $^2S_{1/2}$ — $2p$ $^2P_{3/2}$	192.04	30
$^2S_{1/2}$ — $^2P_{1/2}$	255.10	30

*Blend

Other $\Delta n = 0$ transitions in high-temperature ions are also emitted in the region from 100 to 700 Å. Examples of ions are Ca XVI, Ca XVII, and Ca XVIII of the boron, beryllium, and lithium isoelectronic sequences, respectively. These ions are formed near 6×10^6 K. A list of flare emission lines observed in the NRL Skylab spectroheliograms has recently been published by Dere [24].

In conclusion, high-temperature flare emission lines can be found over an enormous wavelength range. No single instrument can cover this entire range with sufficient spectral, spatial, and time resolution. After the Solar Maximum Mission the region from 80 to 1100 Å will still remain largely unexplored from the standpoint of high spectral and spatial resolution. We now consider the plasma parameters that can be derived from the line intensities and the results for flare plasmas derived from the available solar spectra.

Electron Densities

In the solar atmosphere the excited levels of transition-zone and coronal ions are populated primarily by electron-impact excitation. Density sensitivity of certain spectral line ratios occurs when the rate of depopulation of the excited levels due to collisions $(N_e C_{ij}^d$, where N_e is the electron density and C_{ij}^d is the deexcitation rate coefficient (cm^3/s) between levels i and j) becomes comparable to the spontaneous radiative decay rate A_{ij}. Two cases commonly occur with hypothetical three- and four-level ions. In these two cases application of detailed balance (the number of excitations into a level set equal to the number of deexcitations) leads to the equations for the intensity ratios of lines I_{ij} ($\equiv N_j A_{ji}$). In one case, case A, illustrated at the left in Fig. 2, the equation is

$$\frac{I_{31}}{I_{21}} = \frac{A_{31}(C_{13}/C_{12})}{N_e[(C_{32}C_{13}/C_{12}) + C_{32} + C_{31}] + A_{31}} \quad , \tag{1a}$$

and in the other case, case B, illustrated at the right in Fig. 2, the equations are

$$\frac{N_2}{N_1} = \frac{C_{12} + C_{13}\left(\dfrac{A_{32}}{A_{32} + A_{31}}\right) + C_{14}\left(\dfrac{A_{42}}{A_{41} + A_{42}}\right)}{\dfrac{A_{21}}{N_e} + C_{21} + C_{23}\left(\dfrac{A_{31}}{A_{31} + A_{32}}\right) + C_{24}\left(\dfrac{A_{41}}{A_{41} + A_{42}}\right)} \quad , \tag{1b}$$

$$\frac{I_{42}}{I_{31}} \rightarrow \frac{C_{14}}{C_{13}} \frac{A_{32} + A_{31}}{A_{31}} \quad , \quad N_e \rightarrow 0,$$

$$\frac{I_{42}}{I_{31}} \rightarrow \frac{C_{14} + (\omega_2 C_{24}/\omega_1)}{C_{13}} \frac{A_{32} + A_{31}}{(\omega_2 C_{23}/\omega_1)} \frac{A_{32} + A_{31}}{A_{31}} \quad , \quad N_e \rightarrow N_{eM} \quad .$$
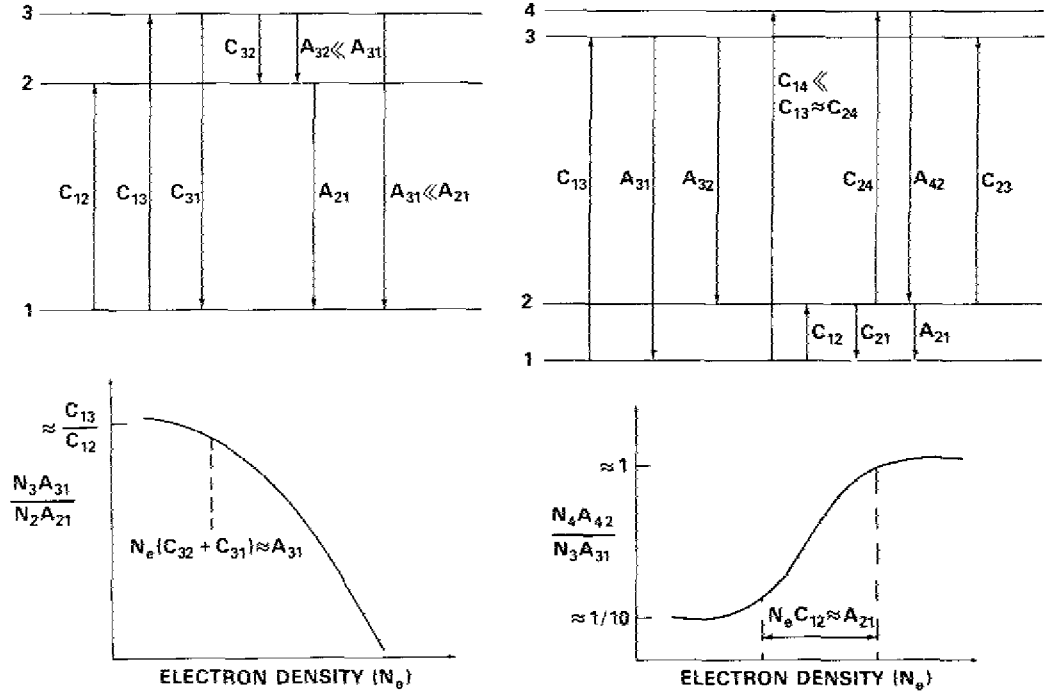
(a) Case A, corresponding to Eq. (1a)   (b) Case B, corresponding to Eqs. (1b)

Fig. 2 — Behavior of density-sensitive line ratios as a function of electron density

These equations contain a number of simplifications that hold for coronal flare ions. For case A we are assuming that $A_{21} \gg A_{31} \gg A_{32}$; that is, level 2 is an allowed level. Also, $A_{21}/N_e C_{12} \gg (C_{ij}/C_{kl})$, where (i,j) and (k,l) are any permutation of the levels 1, 2, and 3. For case B, $N_e C_{34} \ll A_{42}, A_{32}, A_{31}$; also, $A_{41} \ll A_{42}, A_{32}, A_{31}$. That is, level 4 is not easily excited from level 1, so $C_{24} \gg C_{14}$ is also true. An example of this case is level 1 = $^2P_{1/2}$, level 2 = $^2P_{3/2}$, level 3 = $^2D_{3/2}$, and level 4 = $^2D_{5/2}$. The assumptions in case B will hold better for $\Delta n = 0$ transitions than for $\Delta n = 1$ transitions, that is, will hold better when levels 3 and 4 have the same principal quantum numbers as levels 1 and 2. In these equations, ω_2 and ω_1 are the statistical weights of levels 2 and 1, and N_{eM} is defined as the maximum density for which $N_e C_{34}$ may be neglected.

The qualitative behavior of the intensity ratios as a function of density given by the preceding equations is plotted in Fig. 2. For case A the ratio is constant as long as the density-dependent term in the equation (the collisional term) is less than the radiative term $(A_{32} + A_{31})$. Above a certain critical density the collisional and radiative terms become comparable, and when the collisional term dominates, $I_{31}/I_{21} \propto 1/N_e$. This is the density region in which ions of case A are useful as diagnostics. For case B the ratio is constant for both low and high density limits. The case B ratios are useful in the intermediate regime, where they vary with density.

The important point is that some line ratios have density sensitivity because for a certain range of densities collisional depopulation processes are comparable in magnitude to

radiative decay rates. The reason for density sensitivity is fundamentally the same for both case A and case B ions and for other situations that cannot be classified as either purely case A or case B.

Now that we have outlined the principle of density-sensitive line ratios, we may ask which ions possess the right atomic structure to be useful as a density diagnostic in solar flares. The answer is that many ions are available for this purpose, spanning temperatures all the way from the upper chromosphere to coronal flare plasmas. The best way to identify the useful ions is by isoelectronic sequence. The level structure of each ion in a given isoelectronic sequence is the same, so that if a calculation is done for every third or fourth ion of the sequence (preferably those ions of elements abundant in the sun), a clear picture of the possible diagnostics emerges for each sequence. Certain sequences may be ignored, such as the lithium and hydrogen isoelectronic sequences, since at solar densities ($N_e < 10^{15}$ cm^{-3}) no levels are metastable; that is, radiative decay processes are much larger than collisional processes for all excited levels.

By now the following sequences have been investigated in detail: the helium, beryllium, boron, carbon, nitrogen, oxygen, and flourine sequences for ions with configurations $1s^2$ and $2s^2 2p^k$. Thus all ions of the $1s^2$ and $2s^2 2p^k$ configurations for which useful density-sensitive line ratios may exist are now known. The reader is referred to Dere et al. [31] for an application of some of these diagnostics (excluding heliumlike ions) to flare spectra recorded from Skylab. The helium sequence possibilities ($1s^2$) are outlined in many papers, such as by Freeman et al. [32] and Gabriel and Jordan [33].

The situation for the $3s^2 3p^k$ levels is also fairly well in hand. The iron ions from Fe IX through Fe XVII have been studied in detail. The most sensitive ion for flare studies is Fe IX ($3s^2 3p^6$), an example of a case A ion. Line ratios in other ions are not very sensitive to density above $\approx 10^{10}$ cm^{-3}.

Rather than go into the details for every ion useful as a density diagnostic for the solar atmosphere, we have listed comments in Table 2 for those references that are most recent and give results that are useful for flares. We next discuss some of the line ratios particularly useful for flares in terms of the different temperature regions of the thermal flare plasma.

Table 2 — Applications of Density Diagnostics to Solar Flare Spectra

Ref.	Comments
10	This paper reports the density in an x-ray flare burst from the S XV forbidden-to-intersystem line ratio from data obtained with the Columbia x-ray spectrometer on OSO-8: $N_e \geq 10^{14}$ cm^{-3}. The quality of the spectra was poor.
31	This paper reports densities in the 9 Aug. and 17 Dec. 1973 flares (6×10^5 to 6×10^6 K) obtaining $N_e \approx 5 \times 10^9$ to 4×10^{11} cm^{-3} from data recorded with the NRL slitless spectrograph on Skylab. Many lines are affected by blends or plate fogging, but results are overall reliable.

Table continues.

Table 2 (Concluded) — Applications of Density Diagnostics to Solar Flare Spectra

Ref.	Comments
34	This paper reports electron densities in the 9 Aug. 1973 flare (10^5 to 2×10^6 K) determined from data obtained with the NRL slit spectrograph on Skylab. The coronal temperature results are from Dere et al. [31]. For $T \approx 10^5$ K, $N_e \approx 10^{11}$ to 5×10^{12} cm^{-3}. Line ratios such as the O IV ratio $\lambda1407/\lambda1401$, where the wavelengths are in angstroms, are not sufficiently sensitive to give reliable results.
35	This paper reports densities in the 9 Aug. 1973 flare from the Ca XVII line ratio $\lambda233/\lambda193$; $N_e = 5 \times 10^{11}$ cm^{-3} for $T = 6 \times 10^6$ K. The $\lambda233$ line is quite weak.
36	This paper reports densities in flare-type events ($\approx 10^5$ K) from data obtained with the NRL slit spectrograph on Skylab: $N_e = 10^{11}$ to 10^{13} cm^{-3}. The background emission is difficult to separate from dynamical events in several cases.
37	This paper reports the density in a surge observed 20 and 8 seconds above the limb ($\approx 10^5$ K) from data obtained with the NRL slit spectrograph on Skylab: $N_e = 2 \times 10^{10}$ cm^{-3} at 20 seconds and 3.5×10^{11} cm^{-3} at 8 seconds.
38	This paper reports densities in the 15 June 1973 flare ($\approx 10^5$ K) from data obtained with the NRL slit spectrograph on Skylab. The densities in doppler-shifted and stationary components were determined. The values range from $\approx 10^{11}$ to $> 2 \times 10^{13}$ cm^{-3}.
39	This paper reports densities in the 15 June 1973 and 21 Jan. 1974 flares from the Fe IX line ratio $\lambda242/\lambda245$ from data obtained with the NRL slitless spectrograph on Skylab. $N_e = 7 \times 10^{10}$ cm^{-3} for the 15 June flare and $> 2 \times 10^{11}$ cm^{-3} for the 21 Jan. flare.
40	This paper reports densities in the 2 Dec. 1973, 17 Dec. 1973, and 21 Jan. 1974 flares determined from the O IV $\lambda1401$ intersystem line from data obtained with the NRL slit spectrograph on Skylab: $N_e = 4.3 \times 10^{11}$ to 9.2×10^{11} cm^{-3}.
41	This paper reports densities determined in flares observed with the GSFC EUV spectrometer on OSO-5 using the Fe XIX line ratio $\lambda91/\lambda108$ (9×10^6 K): $N_e < 5 \times 10^{13}$ cm^{-3}.
42	This report reports densities in flares observed with the GSFC EUV and x-ray spectrometers on OSO-5 using Fe XXII line ratios (13×10^6 K). The quality of observational data prohibits accurate results, but $N_e < 10^{14}$ cm^{-3}.
43	This paper reports densities in flares observed with the GSFC EUV and x-ray spectrometers on OSO-5 using ratios of Fe XXI lines (10^7 K). The quality of observational data prohibits accurate results, but $N_e < 10^{13}$ cm^{-3}.
44	This paper reports the densities in flares from line ratio of Mg VIII and Si X ($\approx 10^6$ K) from data obtained with the HCO spectrometer on Skylab. The blends are too severe to give reliable results.

The Lower Transition Zone ($T_e \approx 10^5 K$)

The most useful density diagnostics for the lower transition zone fall at wavelengths longer than 1000 Å. The following lines are useful for flares: O I ($\lambda 1355$, $\approx 10^4$ K), Si III ($\lambda 1892$, $\approx 3 \times 10^4$ K), C III ($\lambda 1909$, $\approx 5 \times 10^4$ K), O III ($\lambda 1666$, $\approx 6 \times 10^4$ K), S IV ($\lambda 1406$, $\approx 7 \times 10^4$ K), O IV ($\lambda 1401$, $\approx 1.3 \times 10^5$ K), N IV ($\lambda 1486$, $\approx 1.3 \times 10^5$ K), and O V ($\lambda 1218$, $\approx 2.2 \times 10^5$ K). Their density behavior is similar to case A (Fig. 2). At sufficiently high densities the intensity ratios of these lines to an appropriate allowed line is proportional to $1/N_e$. A practical difficulty exists for these particular lines. For some of the lines (O III, O IV, and N IV) allowed lines are not found at $\lambda > 1000$ Å. The appropriate allowed lines of O IV, for example, fall near 554 Å. However, if the emission measure of the plasma at the temperature of the intersystem lines can be found from allowed lines of other ions, such as C IV and N V for O IV, then the ratio I_{31}/I_{21} of case A can be determined and compared with theory: (For this situation $I_{21} \propto N_e^2 \, \Delta V$, the volume emission measure.) We and Rosenberg [38] first used this technique to determine electron densities in the 15 June 1973 flare observed from Skylab. Problems such as uncertainties in relative element abundances and instrumental calibration can be overcome by using the "normalization" procedure described in Ref. 38.

The ions C III, Si III, and O V have allowed lines for $\lambda > 1000$ Å. Unfortunately they are well separated in wavelength from the intersystem lines for C III and Si III ($\lambda 1176$ and $\lambda 1247$ for C III; $\lambda 1206$ and $\lambda 1298$ for Si III); therefore, at the low temperature at which they are formed, the ratios of the intersystem to the allowed lines are temperature dependent. Also, the separation in wavelength introduces instrumental calibration uncertainties.

The only theoretical work on Si III has been by Nicolas [45]. The temperature problem with Si III is severe for two reasons. First, the contribution function is extremely broad; Si III has an appreciable abundance from 2×10^4 K up to about 6×10^4 K [46]. Second, Tripp et al. [47] have argued that photoionization of Si II will substantially lower the temperature at which the Si III lines are emitted. This effect is density dependent. However, some Si III ratios behave like case B and are not temperature sensitive. One example is $\lambda 1301/\lambda 1296$. Unfortunately the high-density limit is around 10^{11} cm^{-3}, which is rather low for flares.

The ion O V (and also the ion C III) has been studied most recently by Dufton et al. [48]. (The ion C III is one of the best studied from the atomic physics standpoint. Dufton et al. [48] refer to much of the earlier literature on the subject.) The O V ratio $\lambda 1218/\lambda 1371$ should be a useful density diagnostic in flares, but there may be some difficulties due to nonsteady-state processes [38].

Electron densities in flares and flarelike events have been determined from some of these lines by the authors of the references listed in Table 2, and the table summarizes the results. The density behavior of many of the lines is shown in Fig. 3. Densities are seen to be $\geqslant 10^{11}$ cm^{-3} in most cases. The highest density determined is $\geqslant 2 \times 10^{13}$ cm^{-3} for the 15 June flare. The volume of the emitting plasma can be found from the volume emission measures ($N_e^2 \, \Delta V$) and the densities. The volumes are quite small and correspond to characteristic lengths of a few tenths of an arc second. The high densities and long observed lifetimes of the features require constant energy input because of the large radiative energy losses.
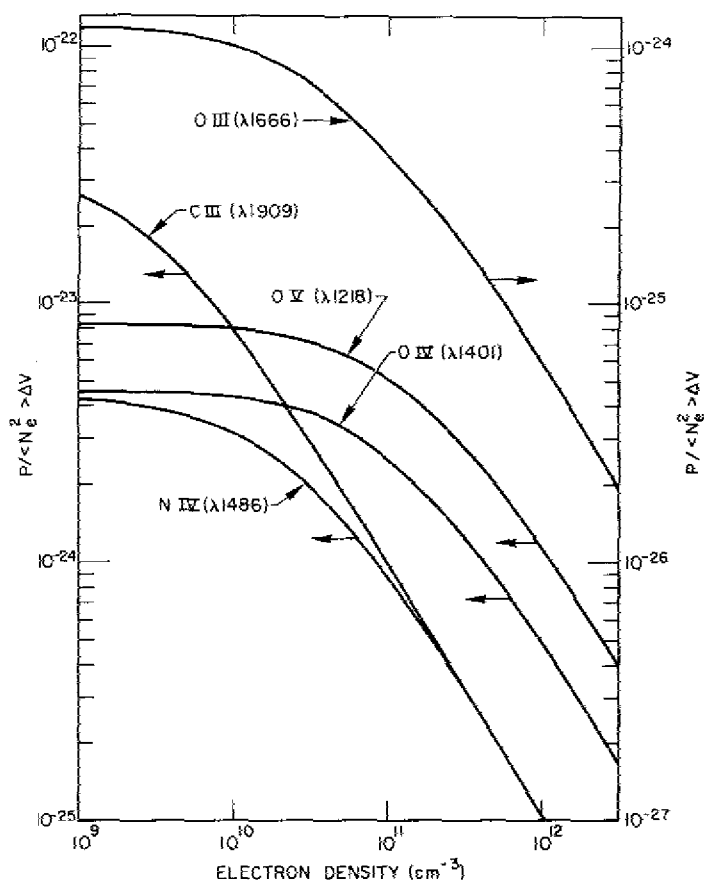
Fig. 3 — The power P ergs-s^{-1} per unit emission measure $\langle N_e^2 \rangle \Delta V$ for intersystem lines longward of 1000 Å produced at temperatures between $\approx 4 \times 10^4$ K and $\approx 2 \times 10^5$ K [37]. These curves have been normalized as described in Refs. 38 and 40.

The Upper Transition Zone ($T_e \approx 6 \times 10^5$ K)

Flare densities in the temperature range of the upper transition zone have not been determined because many of the density-sensitive line ratios fall between 500 and 1000 Å. This region has been extensively observed by the HCO spectroheliometers, but the spectral resolution is too low to allow meaningful measurements. However, many diagnostic possibilities exist.

The Low-Temperature Corona ($T_e \approx 2 \times 10^6$ K)

Many density-sensitive possibilities fall within the wavelength range of the NRL slitless spectrograph flown on Skylab. Recently a rather thorough study of the strongest flares observed has been completed by Dere et al. [31] Unfortunately, many of the possible ratios

belong to case B, and densities in flares are equal to or higher than the high-density limits for many of the ratios. As we mentioned, the most sensitive ratio is the Fe IX pair, $\lambda242/\lambda244$ [39]. For all of the ratios temperature sensitivity is negligible, unlike the case for some of the line ratios of the lower transition zone. The Fe IX ratio behaves like a case A ion (Fig. 4). The best overall isoelectronic sequence for the coronal ions appears to be the C I sequence, although some lines of ions of other sequences are also useful for flares.

Densities determined in flares for quiet coronal temperatures are summarized in at Table 2. The densities are quite high, about two orders of magnitude higher than found in the quiet corona from density-sensitive line ratios of S X [49].

The High-Temperature Flare Plasma ($T_e > 5 \times 10^6$ K)

In some respects the temperature range of the high-temperature flare plasma is the most interesting temperature range for determining densities. The highest temperature flare regions are possibly closer to the site of the initial instabilities that produce flares than the other temperature regions. Unfortunately a difficulty is encountered for this temperature range, regardless of what wavelength range we choose to investigate. The problem is that only highly ionized species exist in the high-temperature regions. As we have seen, the iron ions from Fe XVIII through Fe XXVI are prominent at the highest temperatures. The critical density above which density sensitivity occurs, $N_e^c \approx A_{ij}/C_{ij}$ is relatively high, even for the forbidden lines. For example, in the C I sequence Fe XXI becomes density sensitive between
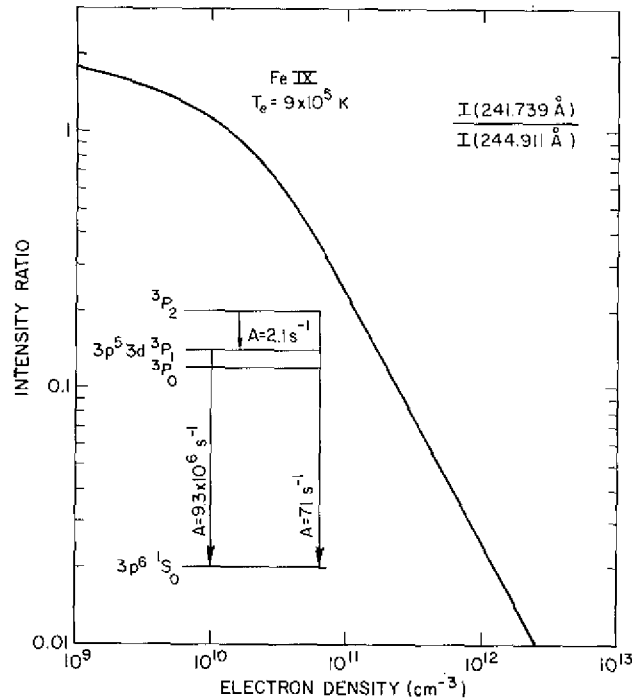

Fig. 4 — The density sensitivity of the Fe IX line ratio, $\lambda242/\lambda245$ [39]

13

$\approx 10^{11}$ and $\approx 10^{14}$ cm^{-3}. For some sequences the highly ionized ions become sensitive for densities that are much higher than actually occur in flares, at least for most of the lifetime of the flare.

We can consider in detail the iron ions from Fe XVIII through Fe XXVI. For Fe XVIII through Fe XXII density sensitivity occurs because of metastable levels of the ground configuration. Table 3 lists the most important of those levels, the total decay rate to all lower levels, and the densities at which collisional depopulation competes with radiative decay. All of these ions are examples of case B. These excited levels are populated in two main ways: by fine structure transitions, such as for Fe XXII ($2s^2 2p\ ^2P_{1/2} \to 2s^2 2p\ ^2P_{3/2}$), and by cascade following excitation to the first excited configuration, such as for Fe XXII ($2s^2 2p\ ^2P_{1/2} + e \to 2s2p^2 \to 2s^2 2p\ ^2P_{3/2} + h\nu$). For the fine-structure excitations, proton excitation as well as electron excitation must be considered.

Some of the iron line ratios become useful only for $N_e \approx 10^{14}$ cm^{-3}. If densities in flares attain these values, then these iron ions will be useful. Although most observations to date indicate that $N_e < 10^{13}$ cm^{-3}, many of the data used to obtain this result are of poor quality, and the time coverage is quite poor. If $N_e < 10^{13}$ cm^{-3}, the best ion for obtaining densities is Fe XXI. This ion has been investigated by Mason et al. [43].

For each of the ions in Table 3, usually several line ratios may be used to obtain densities. A few examples of practical line ratios are also given in Table 3. There are no practical line ratios for Fe XVIII; the ratio of an allowed line to the forbidden line at 974 Å could be used, but the large wavelength difference makes the method difficult from an observational standpoint. For some of the ions x-ray line ratios may be used as well as line ratios in the EUV. However, the crowding together of lines in the x-ray region, which leads to blending, and the fact that $\Delta J = 2$ transitions are in general easier to excite for $\Delta n \neq 0$ transitions than for $\Delta n = 0$ transitions, makes these ratios less useful than their EUV counterparts (J being the total angular momentum, with, for example, $J = 3/2$ for $2s^2 2p\ ^2P_{3/2}$).

Table 3 -- Iron-Line Density Diagnostics

Ion	Level	Decay Rate A (s^{-1})	N_e	Practical Line Ratios (Å)
Fe XVIII	$2s^2 2p^5\ ^2P_{1/2}$	1.92×10^4	$\geqslant 5 \times 10^{13}$	None
Fe XIX	$2s^2 2p^4\ ^1D_2$	1.70×10^4	$\geqslant 10^{12}$	$\lambda 106.33/\lambda 111.70, \lambda 91.02/\lambda 108.37$
Fe XX	$2s^2 2p^3\ ^2D_{5/2}$	$1.69 \times 10^{3*}$	$\approx 10^{10}$ to $\approx 5 \times 10^{12}$	$\lambda 113.36/\lambda 110.64$
Fe XXI	$2s^2 2p^2\ ^3P_2$	8.65×10^2	$\approx 10^{11}$ to $\approx 5 \times 10^{13}$	$\lambda 145.66/\lambda 128.73$
Fe XXII	$2s^2 2p\ ^2P_{3/2}$	$1.39 \times 10^{4*}$	$\approx 10^{12}$ to $\approx 10^{14}$	$\lambda 155.87/\lambda 135.78, \lambda 11.93/\lambda 11.76$
Fe XXIII	$2s2p\ ^3P_2$	9.65×10^3	$\geqslant 10^{14}$	None

*Thanks are given to Dr. H. E. Mason for supplying these decay rates prior to publishing them herself.

The ion Fe XXIII is a more complicated case. The ratio $(2s2p\ ^3P_2 - 2p^2\ ^3P_2)/$ $(2s^2\ ^1S_0 - 2s2p\ ^1P_1)$ is density sensitive for $N_e^c \approx 10^{14}$ cm^{-3}. The point is that the magnetic dipole decay, $2s2p\ ^3P_2 \rightarrow 2s2p\ ^3P_1$, has a much larger rate than the rate of the magnetic quadrupole decay to the ground state, $2s2p\ ^3P_2 \rightarrow 2s^2\ ^1S_0$. However, the ion is probably useless for flares. Most of the iron ions, if not all useful for flares, should be quite useful for tokamak plasmas, where the densities are typically 10^{13} to 10^{14} cm^{-3}.

Fe XXIV is lithiumlike and therefore not useful except for very-high-density laboratory plasmas, where even the allowed levels can be depopulated by collisions. Fe XXVI is similarly not useful for solar plasmas, and the same is true for Fe XXV. The decay rate for the Fe XXV forbidden line, $1s^2\ ^1S_0 - 1s2s\ ^3S_1$, is much too large for flare densities.

The next appreciably abundant element lighter than iron is calcium. Neither Ca XX, Ca XIX, nor Ca XVIII are useful at flare densities. The next two ions, Ca XVII of the beryllium sequence and Ca XVI of the boron sequence, provide good diagnostics. Ca XVII was investigated by Dere and us [35], and Ca XVI was studied by Dere et al. [31]. Ca XVI is a good example of case B, and Ca XVII is similar to Fe XXIII. Ca XV and below are low-temperature ions ($T_e < 5 \times 10^6$ K). Ca XVII and Ca XVI are most abundant at about 6×10^6 K. Abundant elements lighter than calcium are applicable only to $T_e < 6 \times 10^6$ K plasma, which is near the lower boundary of the temperature region we are discussing.

The heliumlike ions present a special case. The density-sensitive lines are found in only the x-ray region. So much has been written about these ions that it would be superfluous to discuss them in detail here. The density-sensitive ratio is $(1s^2\ ^1S_0 - 1s2s\ ^3S_1)/(1s^2\ ^1S_0 - 2s2p\ ^3P_1)$. Complete discussions of these ions can be found in papers by Gabriel and Jordan [33], Gabriel [50], Bhalla, Gabriel and Presnyakov [51], and Presnyakov [52]. Most of the ions are not useful for measuring densities in flares, because N_e^c is too high.

The application of these diagnostics to observations is extremely limited. Most of the flare spectra do not have the spectral resolution to adequately use the diagnostics. However, a few good observations are available, and some of the results are given in Table 2. As can be seen, the densities remain quite high even for the higher temperatures. We believe that the very high densities reported by the Columbia group [10] are questionable. However, we may be wrong, and it will take the Solar Maximum Mission to clarify the issue. Two rather solid observations indicate that $N_e < 10^{14}$ cm^{-3}, at least during the peak x-ray emission of large flares. These observations are that the Fe XXII and the Fe XIX ratios given in Table 3 are near the low-density limit in available flare spectra.

Electron Temperatures and Ionization Equilibrium

Two methods are usually considered for deducing electron temperature in a hot plasma. The first is to use the ratios of dielectronic satellite lines to the resonance lines of heliumlike and hydrogenlike ions in the x-ray region. The second is to use the ratios of two lines in the EUV that originate from two upper levels rather far apart in energy as compared to the thermal energy: $\Delta E / kT_e \gg 1$. The second method depends on the fact that the ratio of the excitation rates of the two lines is proportional to $e^{-\Delta E / kT_e}$.

We demonstrated in Ref. 53 that the second method is not practical. The point is that most ions that produce lines in the EUV are formed over a very narrow temperature range. If the temperature is lowered or raised even by as little as a factor of 2, the contribution functions of the ions decrease by large amounts. Thus large amounts of plasma at the lower or higher temperature must be within the field of view of the instrument in order to produce as much radiation, and thereby be as detectable, as even a small amount of plasma at the ionization equilibrium temperature. Since it is difficult to isolate a structure from contaminating background radiation, even with an instrument with spatial resolution on the order of 1 second, it is probable that measurements of temperatures using the Boltzmann-factor technique will simply confirm the ionization equilibrium temperatures.

By far the best method for determining electron temperature is the method involving dielectronic satellite lines. The method is described in detail by Gabriel [50] and Bhalla, Gabriel, and Presnyakov [51]. Reference 51 is a recalculation of the earlier work of Ref. 50 using revisions of certain atomic data.

Basically, the method takes advantage of the fact that certain x-ray lines are produced by dielectronic recombination to heliumlike and hydrogenlike ions, such as

$$X(1s^2\ ^1S_0) + e \leftrightharpoons X(1s2p^2\ ^2D) \rightarrow X(1s^2 2p\ ^2P) + h\nu.$$
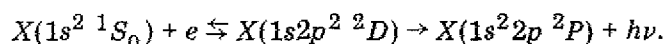
These lines fall close to, and usually on the long wavelength side of, the resonance lines, $1s^2\ ^1S_0 - 1s2p\ ^1P_1$. The intensity ratio of a dielectronic satellite line to the resonance line is approximately given by

$$\frac{I_s}{I_r} = \frac{\alpha_d^s\ N(1s^2\ ^1S_0\ \text{or}\ 1s\ ^2S_{1/2})N_e}{C_{12}^r N(1s^2\ ^1S_0\ \text{or}\ 1s\ ^2S_{1/2})N_e}.$$

Both the population number density N and the electron density N_e drop out of the equation, and the ratio is proportional to simply the ratio of the dielectronic recombination coefficient α_d^s (cm^3/s) to the electron impact excitation coefficient C_{12}^r for the resonance line. This ratio is proportional to $1/T_e$, and the intensity ratio is thereby primarily sensitive to electron temperature.

An additional diagnostic is also available using the satellite lines. Some of the excited satellite levels are metastable to autionization (which is the inverse of dielectronic recombination). The satellite lines resulting from decay of these levels are produced by electron impact excitation of the lithiumlike or heliumlike ions, such as

$$X(1s^2 2s\ ^2S_{1/2}) + e \rightarrow X(1s2s2p\ ^2P) + e' \rightarrow X(1s^2 2s\ ^2S_{1/2}) + h\nu.$$
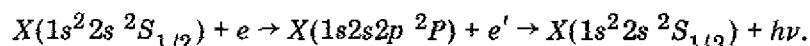
The ratio of these satellite lines to the resonance line is proportional to

$$\frac{I_s}{I_r} = \frac{N_e C_{12}^s\ N(\text{lithiumlike or heliumlike})}{N_e C_{12}^r\ N(\text{heliumlike or hydrogenlike})}.$$

In this case the ratio is primarily proportional to the population ratio of the lithiumlike to the heliumlike ion, or the heliumlike to the hydrogenlike ion. If the electron temperature T_e can be found using a dielectronic satellite, then the satellites produced by innershell excitation enable the departure from ionization equilibrium to be determined.

Although flares have been extensively observed in the x-ray region using Bragg crystal spectrometers [9], only the iron-line spectra [11] obtained by Mandelshtam and his colleagues, and the Mg XII spectrum reported by Aglizki et al. [54], have sufficient spectral resolution to use the satellite line techniques. Unfortunately spectra of only a few large flares were obtained. Temperatures and departures from equilibrium are given in, for example, Presnyakov [52] and Aglizki et al. [54].

The Soviets have used the satellite line technique extensively in diagnosing physical conditions in laser-produced plasmas. At the high densities found in these plasmas $(N_e > 10^{18}$ cm$^{-3})$ some of the satellite line ratios are proportional to electron density as well as to temperature. Earlier laboratory work on the satellites is reviewed in Ref. 55. Examples of recent Soviet work can be found in Bayanov et al. [56] and Boiko, Faenov, and Pikuz [57]. Reference 57 is a comprehensive review. The resolution of the spectra in Ref. 56 is quite high.

More recently workers involved in the tokamak fusion program have become interested in the satellite lines. Extensive calculations and synthetic iron-line spectra have been produced by Robert D. Cowan at Los Alamos Scientific Laboratory. (Also, in connection with the laser-produced plasma fusion program and the solar program, Soviet scientists at the Lebedev Physical Institute have generated a complete set of calculations for all heliumlike and hydrogenlike ions of interest to solar researchers [58].) Tokamak results are described by Hill et al. [59].

As we mentioned, some of the satellite lines can be used to determine departures from ionization equilibrium. Figure 5 shows a potassium spectrum of a laser-produced plasma obtained at NRL. The data are compared with theoretical fits assuming different departures from ionization balance at the electron temperature T_e determined from the dielectronic satellite lines. The temperature T_z is the equilibrium temperature corresponding to the abundance ratio of lithiumlike and heliumlike ions. This ratio is determined from the intensities of some of the innershell satellite lines as we described. In this example the plasma is in a state of transient ionization. The distribution of ions corresponds to a temperature that is about 60% of the actual electron temperature. The same type of analysis can be done for flares using the x-ray spectra to be obtained from the Solar Maximum Mission.

Recently Shapiro and Knight [60] have described a method for investigating departures from ionization equilibrium in the x-ray region. This method is similar in some respects to the method we described for determining the electron temperature. In this case, however, the method is worthwhile, since the contribution functions may be quite large at temperatures far from the equilibrium temperature.

The x-ray experiment planned for the Solar Maximum Mission will have the capability of measuring the intensity of the Fe $K\alpha$ line and similar innershell lines of very low ionization stages of iron. These lines may be produced by fluorescence from thermal coronal x rays or perhaps in certain cases by innershell ionization caused by a high-energy nonthermal
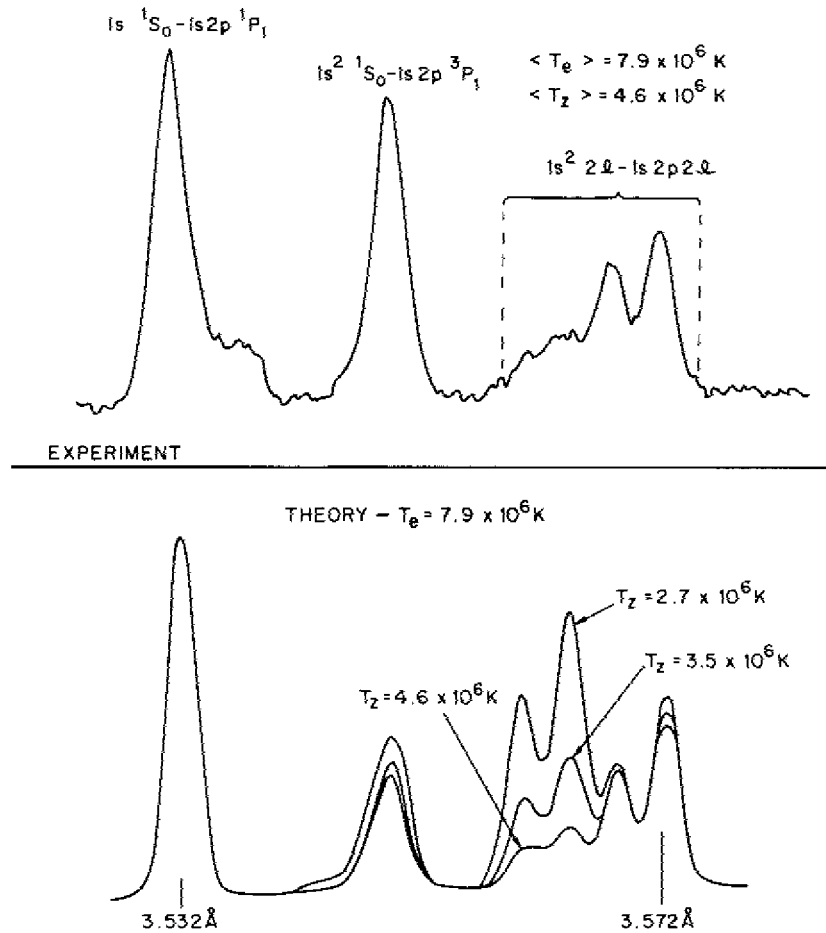
Fig. 5 — Potassium spectrum of a laser-produced plasma obtained at NRL. The electron temperature and "ionization equilibrium temperature" are indicated. Gabriel [50] discusses the "ionization equilibrium temperature."

electron component. In the latter case the intensities of the lines could in principle give information on the high-energy electron spectrum. However, the theory is still in a rudimentary stage, and only low-spectral-resolution data are currently available for the $K\alpha$ line and other nearby innershell lines.

The satellite lines of lithiumlike and heliumlike ions have been extensively investigated, both from the standpoint of spectroscopy (wavelengths and identifications) and theoretical intensities. The x-ray experiment planned for the Solar Maximum Mission will allow the identification of innershell lines emitted from lower stages of ionization, such as berylliumlike ions. Some work was done by us in the laboratory on these satellites using laser-produced plasmas, but the line widths have prevented us from attempting detailed classifications. Figure 6 shows some laser-produced plasma spectra, and Fig. 7 shows the strong
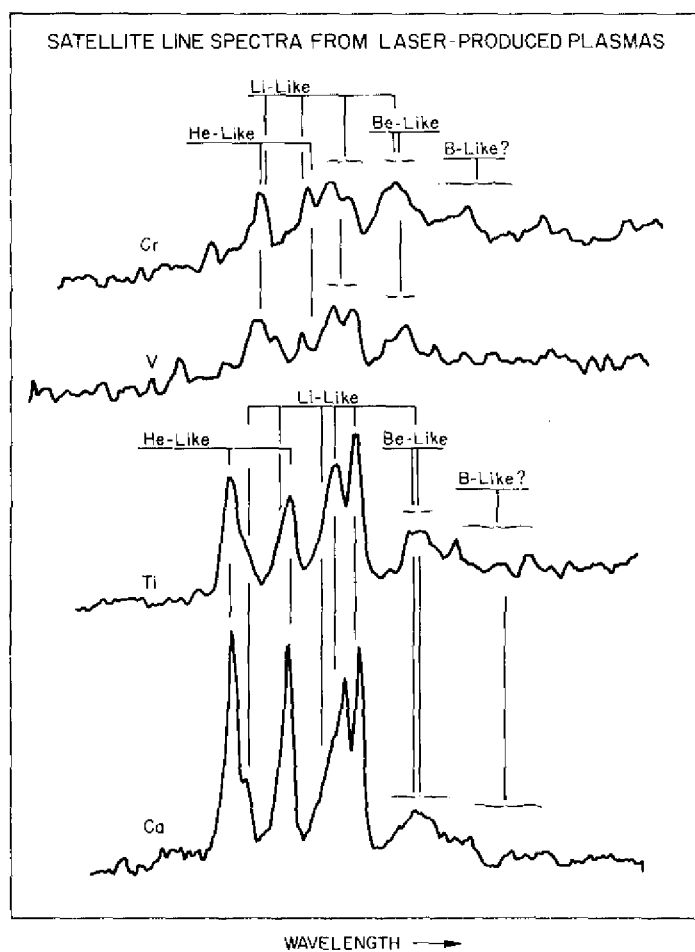
18

Fig. 6 — Laser-produced plasma spectra of the ions shown. Blending of lines of the berylliumlike and boronlike ions makes detailed classifications impossible. The data were obtained with use of the 100-GW glass laser at NRL.

TRANSITION WAVELENGTH (Å)

HELIUMLIKE
$$1s^2\,{}^1S_0 - 1s2p\,{}^1P_1 \quad - \quad 3.176$$
$$1s^2\,{}^1S_0 - 1s2p\,{}^3P_1 \quad - \quad 3.192$$

LITHIUMLIKE
$$\left.\begin{array}{l} 1s^2\,3p - 1s2p\,3p \\ 1s^2\,3s - 1s2p\,3s \end{array}\right\} \quad - \quad 3.181$$
$$1s^2\,2p\,{}^2P_{3/2} - 1s2p^2\,{}^2S_{1/2} \quad - \quad 3.189$$
$$1s^2\,2s\,{}^2S_{1/2} - 1s(2s2p\,{}^1P_1)\,{}^2P_{3/2,\,1/2} \quad - \quad 3.191,\ 3.192$$
$$1s^2\,2s\,{}^2S_{1/2} - 1s(2s2p\,{}^3P)\,{}^2P_{3/2,\,1/2} \quad - \quad 3.200,\ 3.202$$
$$1s^2\,2p^2\,P_{3/2} - 1s2p^2\,{}^2P_{3/2} \quad - \quad 3.203$$
$$1s^2\,2p^2\,P_{1/2,\,3/2} - 1s2p^2\,{}^2D_{3/2,\,5/2} \quad - \quad 3.207,\ 3.210$$
$$1s^2\,2s\,{}^2S_{1/2} - 1s2s2p\,{}^4P_{3/2,\,1/2} \quad - \quad 3.224,\ 3.226$$

BERYLLIUMLIKE
$$1s^2\,2p^2 - 1s2p^3 \quad - \quad 3.221$$
$$3.225 \rightarrow 3.231 \quad <3.228>$$
$$3.233,\ 3.234$$

$$1s^2\,2s2p - 1s2s2p^2 \quad - \quad 3.222$$
$$3.224 \rightarrow 3.225 \quad <3.225>$$
$$3.227 \rightarrow 3.228 \quad <3.228>$$
$$3.229,\ 3.230,\ 3.233 \quad <3.233>$$

$$1s^2\,2s^2 - 1s2s^2\,2p \quad - \quad 3.220$$

Fig. 7 — Theoretical wavelengths of strong x-ray lines of highly ionized calcium. The wavelengths were supplied to us by R. D. Cowan of the Los Alamos Scientific Laboratory.

transitions expected for calcium. The berylliumlike satellites are blended with the lithium-like satellite quartets (lines from the $1s2s2p\,{}^4P$ levels) for calcium; therefore the quartet lines may be difficult to use for estimating departures from ionization equilibrium. During preparation of this report, we became aware of detailed observations and analysis of beryllium-like satellites reported by Boiko et al. [61]. Their spectra are from plasmas produced by Nd and CO_2 lasers.

Emission-Measure Distributions

A quantity that can be derived from the allowed lines is the differential emission measure. The intensity of an allowed line is

$$I_a \propto \int N_e^2\, dV \equiv <N_e^2> \Delta V_{T_m},$$

where ΔV is the approximate volume over which the line is formed. Since many of the spectral lines in the solar atmosphere are formed over narrow temperature ranges, ΔV is

20

interpreted to mean the volume of plasma at average temperature T_m, the temperature at which the contribution function of the line has its maximum. A plot of $<N_e^2> \Delta V$ versus temperature is the so-called differential emission measure. Breaking up ΔV into an area factor a and path length factor Δh by introducing a temperature gradient dh/dT_e is an ad hoc assumption. Differential emission measures plotted as $\int N_e^2 \, dh$ versus T_e are not derived empirically, as sometimes believed. To write $\int N_e^2 \, dh = f(T_e)$, an assumption must be made concerning the area factor. One assumption often employed is that this factor is a constant. Under this assumption Jordan [62] derived $\int N_e^2 \, dh = aT_e^{2.7}$ from quiet-sun data. However, she pointed out that including a reasonable network geometry could reduce the dependence on temperature to $T_e^{3/2}$. There is no very solid empirical evidence for using either of these functional dependences. The only quantity that can be reliably derived from the optically thin lines alone is $<N_e^2> \Delta V$. Even this quantity loses much of its significance if the line in question can be formed over a broad temperature range, as in the cases of Si XIII (6.64 Å) and He II (1640 Å). For these cases it is difficult to give a physical meaning to ΔV.

Recently it has been found that the quantity $<N_e^2> \Delta V$ versus T_e, between $\approx 4 \times 10^4$ K and 2×10^5 K, has much the same shape in many different regions of the solar atmosphere (Fig. 8). In Fig. 8 we have plotted the intensity ratios of the indicated lines to the lines observed in a typical quiet-sun spectrum recorded at 8 seconds above the solar limb [64]. The crosses indicate allowed lines, and the filled circles indicate intersystem lines. The intensities of the allowed lines are proportional to the volume emission measures $<N_e^2> \Delta V$. To within a factor of 2 to 3 the intensity ratios, and therefore ratios of emission measures, are the same for all the different spectra between about 4×10^4 K and 2×10^5 K. The fact that some of the intersystem line ratios in the surge and active region spectra are less than the allowed line ratios indicates a high electron density. Reference 37 is a discussion of this aspect of Fig. 8.

Jordan [64] has suggested that the shape of the emission measure is also the same for temperatures above 10^5 K. If this is found to be the case, Jordan [64] stresses that only one or two measurements of line intensities is necessary to completely define the differential-emission-measure function. There is not yet enough flare data for $T_e > 10^5$ K to assert that the functional dependence of the emission measure is about the same for all flares. This is a problem to be considered with the data from the Solar Maximum Mission.

The usefulness of the differential emission measure acquires real significance only when considered in the context of a particular model. The geometry of the model enables one to reduce ΔV to a path length and area factor. For flares a loop-type geometry seems appropriate in light of the ATM results obtained by NRL and American Science and Engineering. However, we caution against immediately assuming that ΔV can be written as βL, where β is the cross-sectional area of a loop and L is a length along the loop, without first calculating the filling factor f of the loop by using density-sensitive line ratios. A loop volume ΔV at a given temperature can be found using spectra from a slitless spectrograph, but $\Delta V'$ found from the densities and emission measures may be much less than ΔV. One finds out if $\Delta V'$ is less by dividing the volume emission measure by $<N_e^2>$. There is no a priori reason to believe that $f = 1$ for flare loops. For solar loops for which high spatial resolution data exist, such as prominences, $f \ll 1$. Emission-measure distributions in the 9 August 1973 flare using spectral line intensities have recently been published by Underwood et al. [65].
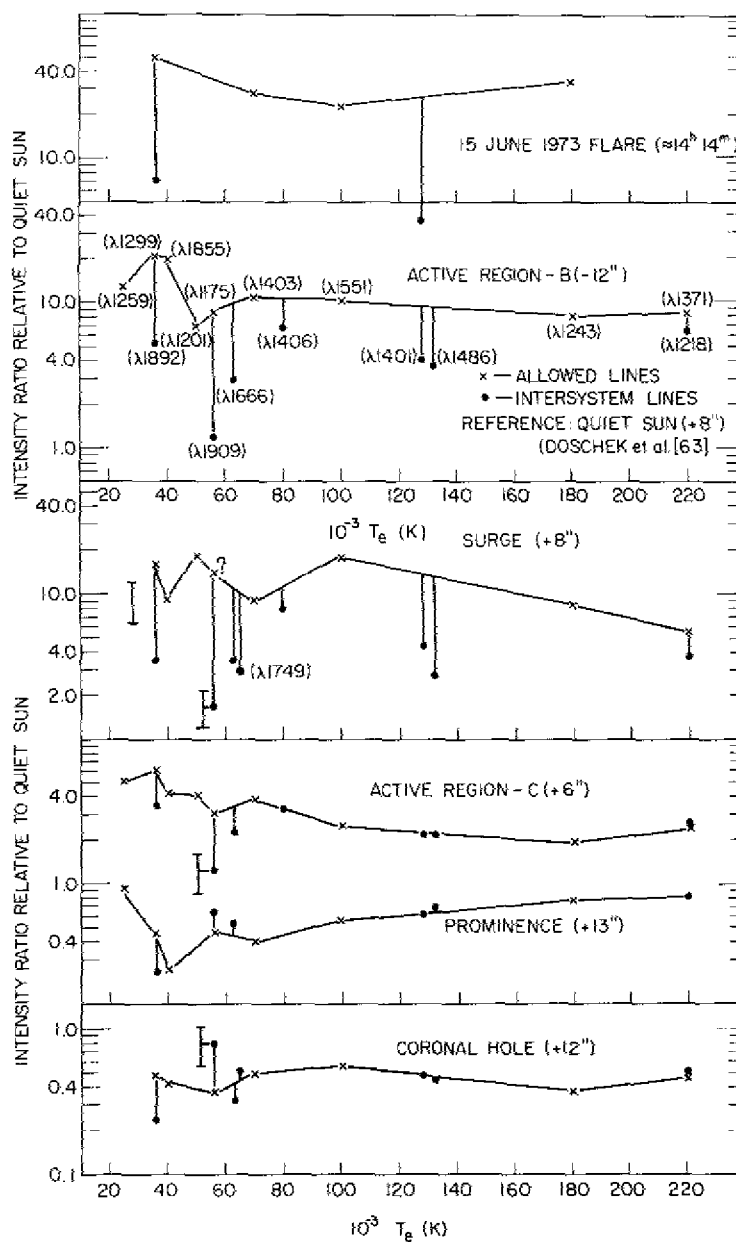
Fig. 8 — Relative intensities of allowed and intersystem lines in different solar regions compared to a typical quiet-sun spectrum observed 8 seconds above the solar limb

A point not stressed in the literature is that interpretation of x-ray satellite-line data may depend rather heavily on the differential emission measure. The reason is that hydrogen-like and heliumlike ions are formed over quite a broad temperature range; therefore contributions to the intensities of resonance lines come from regions at considerably different temperatures. The intensities of satellite lines may be weighted toward different temperatures than the resonance lines, because of the temperature dependences of the excitation processes for these lines.

Line Profiles

In recent years much information has appeared, including Refs. 38, 66, and 67 by us and Rosenberg, concerning the profiles of transition zone lines in flares ($T_e \approx 10^5$ K). At temperatures near 10^5 K in flares, optically thin or effectively thin lines are broadened considerably due to nonthermal mass motions. It is possible that most of the line emission comes from flare-associated surges and sprays. For some events the lines have large Doppler-shifted components as well (≈ 60 to ≈ 200 km/s). In Ref. 36 we show typical examples. The nonthermal velocities ξ giving rise to the broadening have been derived assuming that the shapes of lines are Gaussian, which is a satisfactory approximation in most cases. Then the full width at half-maximum intensity (FWHM) of the line is related to ξ by

$$FWHM = \left[\Delta\lambda_I^2 + 4(ln\ 2)\left(\frac{\lambda}{c}\right)^2 \left(\frac{2kT_i}{M} + \xi^2\right) \right]^{1/2},$$

where $\Delta\lambda_I$ is the instrumental FWHM, T_i is the ion temperature (assumed equal to the electron temperature), M is the ion mass, and the other symbols have the usual meaning. It is difficult to give average values of ξ for flares in the 10^5-K regime, but typical values seem to run from 0 to about 100 km/s. Because of the contamination of the flare profiles with background emission for disk flares, it is essential to determine the profiles of lines, so that emission from physically distinct regions can be separated.

At coronal temperatures of 10^6 K and above, there is little information on ξ for flares. Grineva et al. [11] deduced $\xi = 90$ km/s for the 16 November 1970 event from the width of the 1.85-Å Fe XXV resonance line. Deduced in Ref. 13 is that $\xi \lesssim 60$ km/s at different times during the 15 June 1973 flare from the Fe XXI forbidden line at 1354 Å. From other Fe XXI flare line data it appears that this result is generally true. Another result is that doppler shifts of the centroid of the Fe XXI line are small: $\lesssim 4$ km/s. This is contrary to the case for the transition zone lines. Values of ξ at quiet coronal temperatures ($\approx 1.5 \times 10^6$ K) for flares are not known.

A topic that had not been adequately discussed in the literature is the effect of opacity on flare line profiles for $T_e \geqslant 10^6$ K. (However, a paper on this topic by Acton [67] appeared at the time of this writing.) In Ref. 53 we considered the question briefly. In the present report we consider flares specifically. The problem is impossible to treat in detail without considering specific models. However, we can treat the problem in an approximate way to see if opacity effects can be expected to have a significant influence on line widths.

We consider six typical strong flare lines as examples. The opacity at line center τ_0 can be related to the volume emission measure $\langle N_e^2 \rangle \Delta V$ using the equations

$$\tau_0 = \frac{\sqrt{\pi} e^2}{mc^2} \frac{f \lambda^2}{\Delta \lambda_T} N_I L,$$

$$N_I = \frac{N_I}{N_E} \frac{N_E}{N_H} \frac{N_H}{N_e} N_e,$$

and

$$\Delta \lambda_T = \frac{\lambda}{c} \sqrt{\frac{2k T_{eff}}{M}}.$$

In these equations, f is the oscillator strength, $\Delta \lambda_T$ is the width of the line due to mass motions and thermal doppler broadening without any opacity broadening, N_I is the ion density, L is a characteristic path length along the line of sight (for simplicity we assume $\Delta V = L^3$), N_E is the element density, N_H is the hydrogen density, T_{eff} is an effective temperature (the nonthermal mass motions ξ are interpreted in terms of temperature), and the other symbols have the usual meaning. Combining these equations, we obtain

$$\tau_0 = 6.53 \times 10^{-7} \, f\lambda \, \frac{N_I}{N_E} \frac{N_E}{N_H} \mathcal{M}^{1/2} \, [N_e (\langle N_e^2 \rangle \Delta V)]^{1/3} / T_{eff}^{1/2},$$

where $\mathcal{M}$ is the atomic weight. This equation shows that τ_0 depends rather weakly on $N_e (\langle N_e^2 \rangle \Delta V)$ and T_{eff}.

If opacity is important, spectral lines are broadened beyond their optically thin widths by the transference of photons from the line core into the wings of the line, where they escape from the plasma. The profiles are no longer Gaussian, and their actual shapes can be found only by a rigorous solution of the radiative transfer equations. We may nevertheless gain insight into the effect of opacity on flare line profiles by assuming a constant source function. With use of this approximation the quantity r, defined as the ratio of the FWHM of the optically thin line to the FWHM of the line broadened by opacity, can be calculated. (A Doppler absorption coefficient is used.) The results for six representative lines are given in Table 4. We have assumed a nominal value of $\xi = 50$ km/s for all the calculations and computed τ_0 and r for three values of $\langle N_e^2 \rangle \Delta V$ and two values of N_e. The range of values for $\langle N_e^2 \rangle \Delta V$ are typical for flares; 10^{46} cm^{-3} is typical of a rather small event and 10^{50} cm^{-3} is typical for a fairly large flare. The first density, $N_e = 5 \times 10^{11}$ cm^{-3}, is a value measured for flares. The second density $N_e = 10^{14}$ cm^{-3}, may be achieved for short times during some flares; hence the results with this density have more than academic interest.

The line influenced most by opacity is the Mg IX line. This is because of its comparatively long wavelength and high oscillator strength. (The berylliumlike ions have relatively large oscillator strengths for the singlet transitions, as can be seen by comparing Fe XVIII and Fe XXIII.) For $N_e = 5 \times 10^{11}$ cm^{-3} the amount of excess broadening of the lines due to opacity is less than 15% at each emission measure, except for the Mg IX line. For

Table 4 — Effect of Opacity on Line Widths.
The quantity τ_0 is the opacity at line center, ζ is the nonthermal mass motion,
and r is the ratio of the FWHM of the optically thin line to the FWHM of the
line broadened by opacity.

Line	λ (Å)	$<N_e^2>\Delta V$ (cm^{-3})	τ_0 if $\zeta = 50$ km/s		r	
			$N_e = 5 \times 10^{11}$	10^{14}	5×10^{11}	10^{14}
Fe XXIII ($2s^2\,{}^1S_0$ $- 2s2p\,{}^1P_1$)	133	10^{46}	0.033	0.20	1.0	0.96
		10^{48}	0.16	0.91	0.97	0.86
		10^{50}	0.72	4.2	0.88	0.62
Fe XVIII ($2s^2 2p^5\,{}^2P_{3/2}$ $- 2s2p^6\,{}^2S_{1/2}$)	94	10^{46}	0.011	0.062	1.0	0.99
		10^{48}	0.049	0.29	1.0	0.95
		10^{50}	0.23	1.3	0.96	0.81
Mg IX ($2s^2\,{}^1S_0$ $- 2s2p\,{}^1P_1$)	368	10^{46}	0.34	2.02	0.94	0.74
		10^{48}	1.60	9.4	0.78	0.51
		10^{50}	7.42	43	0.54	0.41
Mg XII ($1s\,{}^2S_{1/2}$ $- 2p\,{}^2P_{1/2,\,3/2}$)	8.42	10^{46}	0.010	0.059	1.0	0.99
		10^{48}	0.047	0.27	1.0	0.95
		10^{50}	0.22	1.3	0.96	0.81
Si XIII ($1s^2\,{}^1S_0$ $- 1s2p\,{}^1P_1$)	6.64	10^{46}	0.048	0.28	1.0	0.95
		10^{48}	0.22	1.3	0.96	0.81
		10^{50}	1.0	6.1	0.85	0.56

emission measures of 10^{48} and 10^{50} cm^{-3}, opacity broadening of the Mg IX line becomes significant. At 10^{14} cm^{-3} significant broadening for all the lines is found for $<N_e^2>\Delta V = 10^{50}$ cm^{-3}. When the opacity becomes large enough, r becomes relatively insensitive to τ_0. For example, for Mg IX and $N_e = 10^{14}$ cm^{-3}, values of τ_0 of 9.4 and 43 correspond to values of r of 0.51 and 0.41.

These results indicate that opacity may be an important factor for some lines like Mg IX, even for densities between 10^{11} and 10^{12} cm^{-3}. If r can be found, for example by comparing the widths of allowed and intersystem lines, then the product $[N_e(<N_e^2>\Delta V)]^{1/3}$ $\equiv N_e L$ can be found from the preceding equation for τ_0, if a constant source function is assumed. If the density is known from line-ratio techniques, then an estimate of L can be obtained. This result will be most accurate for small τ_0, for the reason mentioned in the preceding paragraph.

25

CONCLUSIONS

Our discussion shows that a wide range of spectral diagnostics is available for the study of solar flares. These diagnostics are based on measurements of the intensities of spectral lines and determinations of spectral line shapes. After the Solar Maximum Mission the spectral region from about 40 to about 1000 Å will still be largely unexplored. This statement may sound somewhat surprising in view of the amount of data already accumulated in this spectral range from the instruments flown by HCO and NRL on unmanned spacecraft and on Skylab. However, in view of the low spectral resolution of the HCO spectrometers and the overlapping of images in the NRL spectroheliograms, it is difficult, if not in many instances impossible, to extract accurate quantitative information from these data.

The overlapping of the NRL spectroheliogram images is a well-known deficiency of the NRL slitless spectrographs. Less well-appreciated is that the HCO spectrometers have such low spectral resolution that virtually every feature observed in the spectrum is actually a blend of lines. Only the intensities of the very strongest lines may be accurately determined. It is impossible to apply any of the recently developed density diagnostics to the data, and measurements of profiles of lines are far beyond the capabilities of the instrument.

Recently we have constructed a synthetic solar-emission-line spectrum for the spectral region from 80 to 800 Å. We have used all the currently available spectroscopic and atomic data and have included most of the expected strong lines. Specific solar models can be incorporated into the spectrum, and the lines can be plotted with any desired spectral resolution. This synthetic spectrum will be continually updated as new spectroscopic and atomic data become available.

It is useful to conclude by illustrating some of the differences in the solar flare spectrum near 100 Å produced by variations in electron density, using the synthetic spectrum. For this illustration we assume a linear increase of emission measure with temperature, up to about 20×10^6 K, the temperature of formation of Fe XXIV. Thus the spectrum chosen for illustration is similar to a flare spectrum. We show the portion of the spectrum from 90 to 180 Å in Fig. 9, for three values of the electron density: 10^9, 10^{11}, and 10^{13} cm^{-3}. The spectrum is dominated by emission lines of highly ionized iron. Two strong lines of Fe XXI appear in the 10^{13}-cm^{-3} spectrum that are much weaker in the 10^{11}-cm^{-3} spectrum and absent in the 10^9-cm^{-3} spectrum. There is also an Fe XXI line not sensitive to density variations. These lines are marked by arrows. Other weak lines also appear in the 10^{13}-cm^{-3} spectrum that are absent in the lower density spectra. Emission measures can be determined from the allowed lines not sensitive to density, densities can be found from suitable line ratios, and nonthermal motions can be found from line profiles. The value of such spectra for analyzing physical conditions in solar flare plasmas is apparent. This illustration also shows clearly why high spectral resolution is essential, if the diagnostics we have been discussing are to be seriously applied to solar data. The lines have been plotted assuming thermal doppler broadening and a random nonthermal velocity of 20 km/s.

Our comments have been rather critical of some of the solar instrumentation flown in the past. However, it is easier to be critical with hindsight than with foresight. Although not possessing the degree of spectral resolution that we desire, the data from these instruments and others have enabled us to achieve much of our current understanding of the upper solar
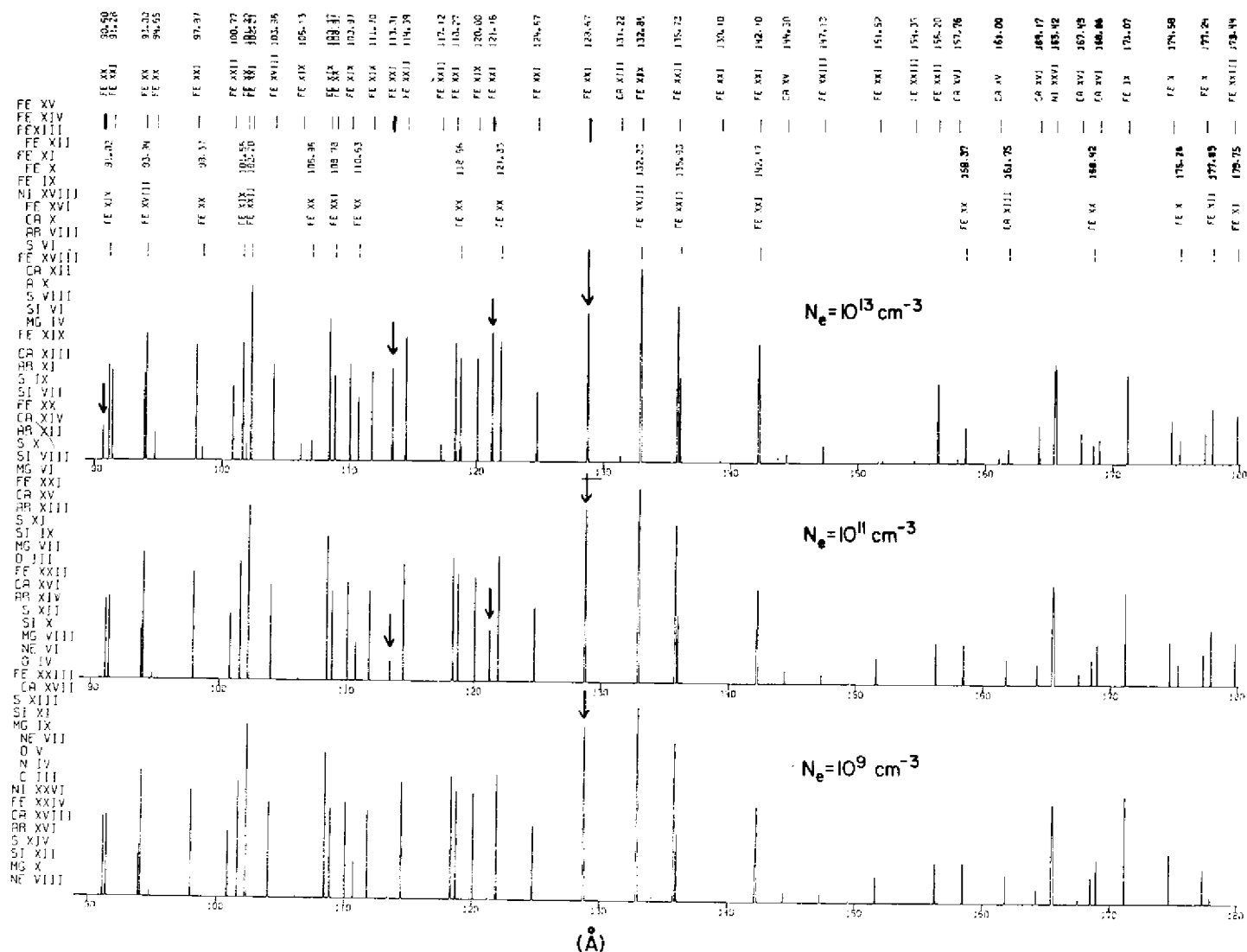
Fig. 9 — Synthetic spectra between 80 and 120 Å. Most of the lines are due to transitions in Fe XVIII through Fe XXIII. The arrows indicate lines of Fe XXI useful for electron-density determinations in solar flares. The listing of ions to the left of the spectra show the ions included in the entire synthetic spectrum, which covers the range from 80 to 800 Å. The line widths are determined by thermal doppler broadening and a 20-km/s nonthermal broadening due to random mass motions. Wavelengths in the figure are given in Angstrom units.

atmosphere. We will now enter into a new era of solar space research, based on the availability of the space shuttle. We hope that our knowledge of the sun and its environment will continue to increase at the same rate as it has in the last 30 years.

REFERENCES

1. J-D.F. Bartoe, G.E. Brueckner, J.D. Purcell, and R. Tousey, Applied Optics 16, 879 (1977.)

2. R. Tousey, J-D.F. Bartoe, G.E. Brueckner, and J.D. Purcell, Applied Optics 16, 870 (1977).

3. K.G. Widing and K.P. Dere, Solar Phys. 55, 431 (1977).

4. E.M. Reeves, M.C.E. Huber, and J.G. Timothy, Applied Optics 16, 837 (1977).

5. W.E. Behring, L. Cohen, and U. Feldman, Astrophys. J. 175, 493 (1972).

6. S.O. Kastner, W.M. Neupert, and M. Swartz, Astrophys. J. 191, 261 (1974).

7. W.M. Neupert, W. Gates, M. Swartz, and R. Young, Astrophys. J. (Letters) 149, L79 (1967).

8. W.M. Neupert, M. Swartz, and S.O. Kastner, Solar Phys. 31, 171 (1973).

9. G.A. Doschek, Space Science Reviews 13, 765 (1972).

10. J.H. Parkinson, H.L. Kestenbaum, K.S. Long, and R. Novick, *Proceedings of the Nov. 7-10, 1977, OSO-8 Workshop*, pub. by Univ. of Colorado, 1977.

11. Yu. I. Grineva, V.I. Karev, V.V. Korneev, V.V. Krutov, S.L. Mandelstam, L.A. Vainstein, D.N. Vasilyev, and I.A. Zhitnik, Solar Phys. 29, 441 (1973).

12. V.A. Boiko, Y.P. Voinov, V.A. Gribkov, and G.V. Sklizkov, Optics and Spectrosc. 29, 1023 (1970).

13. G.A. Doschek, U. Feldman, K.P. Dere, G.D. Sandlin, M.E. VanHoosier. G.E. Brueckner, J.D. Purcell, and R. Tousey, Astrophys. J. (Letters) 196, L83 (1975).

14. E.Ya. Kononov, A.N. Ryabtsev, U.I. Safronova, and S.S. Churilov, J. Phys. B 9, L477 (1976).

15. U. Feldman, G.A. Doschek, D.J. Nagel, W.E. Behring, and L. Cohen, Astrophys. J. (Letters) 183, L43 (1973).

16. B.C. Fawcett, M. Galanti, and N.J. Peacock, J. Phys. B. 7 1149 (1974).

17. K.G. Widing, *Astrophys. J.* 222, 735 (1978).

18. C. Jordan, in *Progress in Atomic Spectroscopy*, edited by Handle and H. Kleinpoppen, Pleunum, New York; 1977. The wavelength is from Ref. 16.

19. G.A. Doschek, U. Feldman, R.D. Cowan, and L. Cohen, Astrophys. J. 188, 417 (1974).

20. E.Ya. Kononov, K.N. Koshelev, L.I. Podabedova, S.V. Chekalin, and S.S. Churilov, J. Phys. B 9, 565 (1976).

21. U. Feldman, G.A. Doschek, R.D. Cowan, and L. Cohen, Astrophys. J. 196, 613 (1975).

22. G.A. Doschek, U. Feldman, J. Davis, and R.D. Cowan, Phys. Rev. A 12, 980 (1975).

23. S. Suckewer, and E. Hinnov, Phys. Rev. Letters 41, 756 (1978).

24. K.P. Dere, Astrophys. J. 221, 1062 (1978).

25. G.A. Doschek, U. Feldman, and L. Cohen, J. Opt. Soc. Am. 65, 463 (1975).

26. B.C. Fawcett, and R.D. Cowan, Monthly Not. R. Astr. Soc. 171, 1 (1975).

27. G.D. Sandlin, G.E. Brueckner, V.E. Sherrer, and R. Tousey, Astrophys. J. (Letters) 205, L47 (1976).

28. R.W. Noyes, in *High Energy Phenomena on the Sun*, edited by R. Ramaty and R. G. Stone, NASA SP-342, 1973.

29. K.G. Widing, Astrophys. J. (Letters) 197, L33 (1975).

30. W.M. Neupert, Phil. Trans. Roy. Soc. London A 270, 143 (1971).

31. K.P. Dere, H.E. Mason, K.G. Widing, and A.K. Bhatia, Astrophys. J., submitted 1978.

32. F.F. Freeman, A.H. Gabriel, B.B. Jones, and C. Jordan, Phil. Trans. Roy. Soc. London A270, 127 (1971).

33. A.H. Gabriel, and C. Jordan, *Case Studies in Atomic Collision Physics*, Vol. 2, edited by E. W. McDaniel and M. C. McDowell, Amsterdam, North-Holland, 1972.

34. K.P. Dere and J.W. Cook, Astrophys. J. 229, 772 (1979).

35. G.A. Doschek, U. Feldman, and K.P. Dere, Astron. and Astrophys. 60, L11 (1977).

36. G.A. Doschek and U. Feldman, Astronomy and Astrophys. 69, 11 (1978).

37. G.A. Doschek, U. Feldman, and H.E. Mason, Astronomy and Astrophys. in press (1979).

38. U. Feldman, G.A. Doschek, and F.D. Rosenberg, Astrophys. J. 215, 652 (1977).

39. U. Feldman, G.A. Doschek, and K.G. Widing, Astrophys. J. 219, 304 (1978).

40. U. Feldman and G.A. Doschek, Astronomy and Astrophys. 65, 215 (1978).

41. M. Loulergue and H. Nussbaumer, preprint, 1978.

42. H.E. Mason and P.J. Storey, preprint, 1978.

43. H.E. Mason, G.A. Doschek, U. Feldman, and A.K. Bhatia, Astron. and Astrophys. 73, 74 (1979).

44. J.E. Vernazza and H.E. Mason, Astrophys. J. 226, 720 (1978).

45. K.R. Nicolas, Ph.D. thesis, Univ. of Maryland, 1977.

46. C. Jordan, Monthly Notices Roy. Astron. Soc. 142, 501 (1969).

47. D.A. Tripp, R.G. Athay, and V.L. Peterson, Astrophys. J. 220, 314 (1978).

48. P.L. Dufton, K.A. Berrington, P.G. Burke, and A.E. Kingston, Astron. and Astrophys. 62, 111 (1978).

49. U. Feldman, G.A. Doschek, J.T. Mariska, A.K. Bhatia, and H.E. Mason, 1978, Astrophys. J. 226, 674 (1978).

50. A.H. Gabriel, Monthly Notices Roy. Astron. Soc. 160, 99 (1972).

51. C.P. Bhalla, A.H. Gabriel, and L.P. Presnyakov, Monthly Notices Roy. Astron. Soc. 172, 359 (1975).

52. L.P. Presnyakov, Sov. Phys. Usp. 19, 387 (1976).

53. U. Feldman, and G.A. Doschek, Space Science Reviews 22, 191 (1978).

54. E.V. Aglizki, V.A. Boiko, A.Ya. Faenov, V.V. Korneev, V.V. Krutov, S.L. Mandelstam, S.A. Pikuz, U.I. Safranova, J.A. Sylwester, A.M. Urnov, L.A. Vainshtein, and I.A. Zhitnik, Solar Phys. 56, 375 (1978).

55. G.A. Doschek, pp 165-181 in *Solar Gamma-, X-, and EUV Radiation*, IAU Symposium 68, edited by S.R. Kane, Reidel Publ. Co., 1975.

56. V.I. Bayanov, S.S. Gulidov, A.A. Mak, G.V. Peregudov, I.I. Sobelman, A.D. Starikov, and V.A. Chirkov, Sov. J. Quant. Electr. 6, 1226 (1976).

57. V.A. Boiko, A.Ya. Faenov, and S.A. Pikuz, J. Quant. Spectrosc. Radiat. Transfer 19, 11 (1978).

58. A.M. Urnov, private communication, 1978.

59. K.W. Hill, S. von Goeler, M. Bitter, L. Campbell, R.D. Cowan, B. Fraenkel, A. Greenberger, R. Horton, J. Hovey, W. Roney, N. Sauthoff, and W. Stodiek, Princeton Univ. Plasma Physics Lab preprint PPPL-1457, 1978.

60. P.R. Shapiro, and J.W. Knight, Astrophys. J. 224, 1028 (1978).

61. V.A. Boiko, A.Yu. Chugunov, T.G. Ivanova, A.Ya. Faenov, I.V. Holin, S.A. Pikuz A.M. Urnov, L.A. Vainshtein, and U.I. Safronova, Monthly Notices Roy. Astron. Soc. 185, 305 (1978).

62. C. Jordan, Phil. Trans. Roy. Soc. Lond. A. 281, 391 (1976).

63. G.A. Doschek, U. Feldman, M.E. VanHoosier, and J-D.F. Bartoe, Astrophys. J. Suppl. 31, 417 (1976).

64. C. Jordan, 1978, in preparation

65. J.H. Underwood, S.K. Antiochos, U. Feldman, and K.P. Dere, Astrophys. J. 224, 1017 (1978).

66. G.A. Doschek, U. Feldman, and F.D. Rosenberg, Astrophys. J. 215, 329 (1977).

67. L.W. Acton, Astrophys. J. 225, 1069 (1978).